

Signatures of quantum phase transitions after quenches in quantum chaotic one-dimensional systems

Asmi Haldar,¹ Krishnanand Mallayya,² Markus Heyl,³ Frank Pollmann,⁴ Marcos Rigol,² and Arnab Das¹

¹*Indian Association for the Cultivation of Science (School of Physical Sciences),
2A & 2B Raja S. C. Mullick Road, Kolkata 700032, India*

²*Department of Physics, The Pennsylvania State University, University Park, Pennsylvania 16802, USA*

³*Max Planck Institute for the Physics of Complex Systems,
Nöthnitzer Straße 38, D-01187, Dresden, Germany*

⁴*Department of Physics, Technische Universität München,
James-Frank-Str. 1/I 85748 Garching b. München, Germany*

Quantum phase transitions are central for the understanding of the equilibrium low-temperature properties of quantum matter. Locating them can be challenging both by means of theoretical techniques as well as for experiments. Here, we show that the antithetic strategy of forcing a system strongly out of equilibrium can provide a route to identify signatures of quantum phase transitions. By quenching a quantum chaotic (nonintegrable) spin chain, we find that local observables can exhibit distinct features in their intermediate-time dynamics, when the quench parameter is close to its critical value, where the ground state undergoes a quantum phase transition. We find that the effective temperature in the expected thermal-like states after equilibration exhibits a minimum in the vicinity of the quantum critical value of the quench parameter, correlating with the features in the real-time dynamics of observables. We also explore dynamical nonequilibrium signatures of a quantum critical point in a model with a topological transition, and discuss how to access our results experimentally in systems of Rydberg atoms.

I. INTRODUCTION

Quantum phase transitions constitute a key concept for the perception and description of the low-temperature properties of quantum many-body systems ranging across various branches in physics from quantum magnets, high-temperature superconductivity, neutron stars, to the quark-gluon plasma [1, 2]. The microscopic description of the underlying complex many-body models can, however, be challenging theoretically. Quantum simulators promise to overcome such challenges by experimental means through providing pristine and controllable realizations of the respective microscopic models [3, 4]. Importantly, many of these quantum simulator platforms provide access to real-time dynamics, which has been very recently used to identify unique real-time aspects of quantum phase transitions in a system of Rydberg atoms by probing the Kibble-Zurek mechanism of universal defect production for slow parameter sweeps [5]. Recent theoretical works have provided evidence that nonequilibrium quantum evolution can be utilized to probe quantum phase transitions in integrable systems [6, 7], in prethermal states for models close to integrability [8], or through out-of-time-order correlators [9]. However, identifying real-time signatures of quantum phase transitions in generic quantum chaotic many-body systems accessible within current experimental technology has remained a challenge.

In this work we show that ergodic quantum matter can exhibit dynamical signatures of quantum phase transitions by the antithetic strategy of forcing these systems far out of equilibrium and therefore beyond the ground state manifold. We find that the intermediate-time dynamics of local observables and the entanglement entropy

exhibit distinct features after quantum quenches in the anisotropic next-nearest neighbor Ising (ANNNI) chain upon tuning the quench parameter across an underlying quantum phase transition. We observe that the derivatives of these quantities with respect to the quench parameter develop strong dips/peaks in the vicinity of the quantum phase transition. We determine the quantum real-time evolution by means of the infinite-Time Evolved Block Decimation (iTEBD), which provides numerically exact results for the transient to intermediate-time dynamics in the thermodynamic limit [10–12].

In order to access the asymptotic long-time properties of the considered quantum chaotic system after the expected thermalization, we employ a numerical linked cluster expansion (NLCE) for thermal equilibrium states [13]. Most importantly, we again find distinct signatures of the quantum phase transition in derivatives of the correlation functions. Also, the effective temperature exhibits a marked minimum as function of the quench parameter in close vicinity to the quantum phase transition. Since the considered one-dimensional system does not support singular behavior after equilibration, upon assuming that eigenstate thermalization occurs [14–17], these prominent features are not associated with nonanalytic properties (in contrast to the integrable systems studied in Refs. [6, 7]), but nevertheless represent distinct signatures of quantum phase transitions. Finally, we discuss similar phenomena for a quantum phase transition in a model with a topological transition. We also discuss how our findings can be accessed experimentally with current technology in systems of Rydberg atoms.

The presentation is organized as follows. In Sec. II, we introduce the Hamiltonian of the ANNNI chain, and introduce the protocol used to probe the ferromagnetic

to paramagnetic quantum phase transition via dynamics following quantum quenches. The results obtained for dynamics after the quenches are presented in Sec. III, while the results after thermalization are presented in Sec. IV. Combining results from the dynamics and thermalization, in Sec. V we report the estimated phase diagram for the ferromagnetic to paramagnetic quantum phase transition for a wide range of parameters of the ANNNI chain. In Sec. VI we summarize our results, discuss their implications, and report evidence of qualitatively similar behavior in the short-time dynamics after quenches across a topological transition.

II. ANNNI HAMILTONIAN AND QUENCH PROTOCOL

The ANNNI chain is a very well studied spin model (see, e.g., Ref. [18]). Its Hamiltonian in a chain with L sites can be written as

$$\hat{H} \doteq - \sum_i^L \sigma_i^x \sigma_{i+1}^x + \kappa \sum_i^L \sigma_i^x \sigma_{i+2}^x - \Gamma \sum_i^L \sigma_i^z. \quad (1)$$

When mapped onto a fermionic Hamiltonian using Jordan-Wigner transformation [19], the next-nearest-neighbor term (with strength κ) maps onto a four-fermion interaction. At $T = 0$, this model has a rich (and still partly controversial) phase diagram in the κ - Γ plane. The quantum phase transition line from the ferromagnetic to the paramagnetic phase, which occurs as the antiferromagnetic next-nearest neighbor coupling $\kappa > 0$ crosses a critical value for a fixed $|\Gamma| < 1$, is a second order phase transition (see, e.g., Ref. [20]). In the quadrant ($\kappa > 0, \Gamma > 0$), this line is well described using second order perturbation theory, with the critical parameters satisfying (see Fig. 11) [20]:

$$1 - 2\kappa_c = \Gamma_c - \Gamma_c^2 \frac{\kappa_c}{2(1 - \kappa_c)}. \quad (2)$$

To probe this ferromagnetic to paramagnetic quantum phase transition at a fixed value of Γ , we generate a family of Hamiltonians $\hat{H}(\kappa)$. We then generate a family of nonequilibrium states via quenches with $\hat{H}(\kappa)$. The protocol (straightforward to generalize to other models) consists of following steps (see Fig. 1):

- (i) The initial state is fixed to be the ground state $|\psi(\kappa_I)\rangle$ of $\hat{H}(\kappa_I)$, where κ_I is deep in the ferromagnetic phase.
- (ii) We suddenly change (quench) $\kappa_I \rightarrow \kappa$ at $t = 0$, and study the unitary time evolution of the system under the time-independent Hamiltonian $\hat{H}(\kappa)$, so that $|\psi(t, \kappa)\rangle = \exp[-i\hat{H}(\kappa)t]|\psi(\kappa_I)\rangle$, where we have set $\hbar = 1$.
- (iii) We compute expectation values of observables $\mathcal{O}(t, \kappa) = \langle \psi(t, \kappa) | \hat{\mathcal{O}} | \psi(t, \kappa) \rangle$.

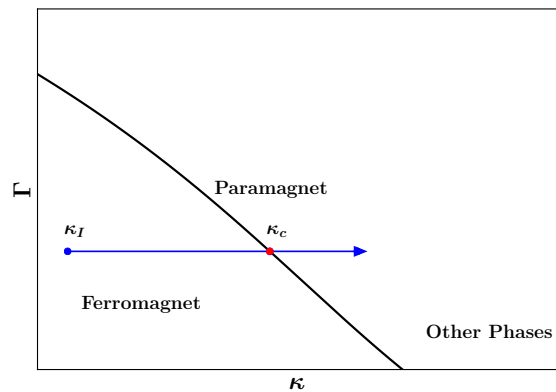


FIG. 1. Schematic representation of our quench protocol, superimposed on a schematic ground-state phase diagram of the ANNNI chain.

- (iv) For a fixed value of t , we study how $\mathcal{O}(t, \kappa)$ changes with κ , focusing on the behavior in the vicinity of κ_c , where κ_c is the critical value of κ for the transition given the selected value of Γ .

III. QUANTUM DYNAMICS

Here we study the time evolution of observables after quantum quenches in the infinite ANNNI chain, which we compute using iTEBD [10–12]. Following the protocol introduced in Sec. II (see Fig. 1), we fix Γ (we take $\Gamma = 0.2$) and then fix κ_I so that the initial state is a ground state of the ANNNI chain deep in the ferromagnetic phase (we take $\kappa_I = 0$). In our iTEBD calculations, we introduce a very small ($\sim 10^{-6}$) longitudinal field to pin one of the two degenerate maximally polarized ground states. The critical value of κ for the ferromagnetic to paramagnetic quantum phase transition for $\Gamma = 0.2$ is $\kappa_c \approx 0.41$.

We first focus on the dynamics of two local observables, the nearest and next nearest neighbor longitudinal correlators

$$C_{1(2)}^x = \frac{1}{L} \sum_{i=1}^L \langle \sigma_i^x \sigma_{i+1(2)}^x \rangle. \quad (3)$$

In Fig. 2, we show results for the time evolution of C_1^x [Fig. 2(a)] and C_2^x [Fig. 2(b)] for six values of κ after the quench. The dynamics of both longitudinal correlators is qualitatively similar for the values of κ shown. Their decrease with time speeds up as κ increases about κ_c . How the closeness to κ_c affects the dynamics is better seen by plotting the correlations for fixed times t after the quench as functions of κ [step (iv) in the protocol introduced in Sec. II]. This is done in Fig. 3, where we show results for C_1^x [Fig. 3(a)] and C_2^x [Fig. 3(b)]. At all times reported, C_1^x and C_2^x decrease rapidly with increasing the value of κ for $\kappa \gtrsim \kappa_c$. In addition, with increasing time, the decrease in the correlators becomes more prominent when

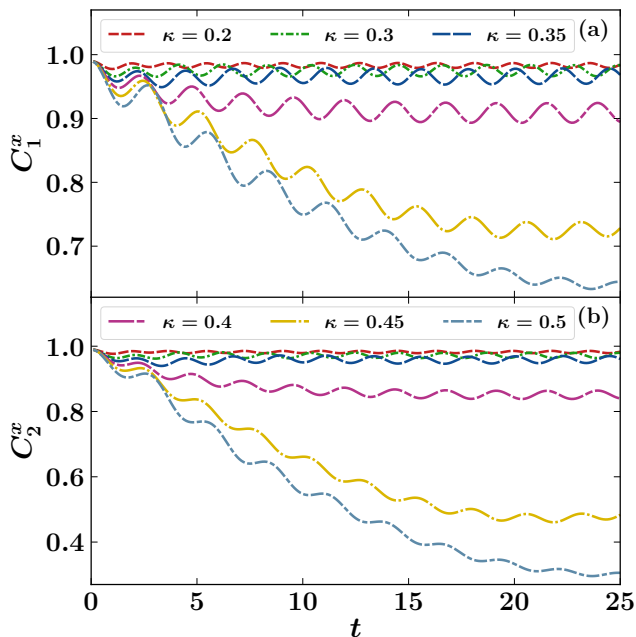


FIG. 2. Time evolution of (a) C_1^x and (b) C_2^x for six values of κ after quenches starting from the ground state of the ANNNI Hamiltonian with $\Gamma = 0.2$ and $\kappa_I = 0$.

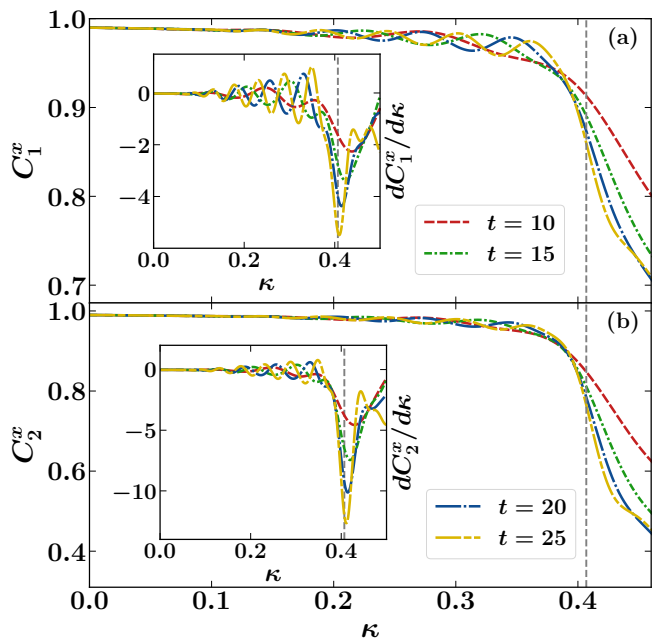


FIG. 3. Ferromagnetic to paramagnetic quantum phase transition in the ANNNI chain as revealed via real time dynamics of local observables. (a) C_1^x and (b) C_2^x at different times plotted as functions of κ after the quench (the legend is the same for both observables). (Insets) Derivative with respect to κ of the results shown in the main panels. The initial state is the ground state of the ANNNI Hamiltonian with $\Gamma = 0.2$ and $\kappa_I = 0$. The vertical dashed lines mark the critical $\kappa_c \approx 0.41$.

$\kappa \approx \kappa_c$. This is better seen in the insets, where we show the derivative of the correlators. They develop sharper dips close to κ_c as the evolution time increases.

In Refs. [6, 7] it was proved that following the same protocol discussed here but for noninteracting models (or models mappable to them) results in nonanalytic behavior of local observables at the quantum phase transition in the limit $t \rightarrow \infty$ (after having taken the thermodynamic limit first). While this is not the case in the quenches in generic models studied here (see Sec. IV), the prominent features seen in Fig. 3 at finite times are promising for an experimental determination of κ_c .

We also studied the dynamics of the half chain entanglement entropy $S_{1/2} = -\text{Tr}[\rho_{1/2} \ln \rho_{1/2}]$, where $\rho_{1/2}$ is the density matrix of the half chain (obtained by tracing out the other half). This is a nonlocal observable that is expected to increase linearly with time in quantum chaotic systems [21]. In Fig. 4(a), we plot the time evolution of $S_{1/2}$ for six values of κ . As for the local operators in Fig. 2(a), the change of $S_{1/2}$ with time speeds up as κ increases about κ_c . Figure 4(b) shows $S_{1/2}$ at fixed times t after the quench plotted vs κ , and the inset in Fig. 4(b) shows the derivative with respect to κ of the results in the main panel. Like the local operators in Fig. 3, the behavior of the half chain entanglement entropy carries a marker of the quantum phase transition.

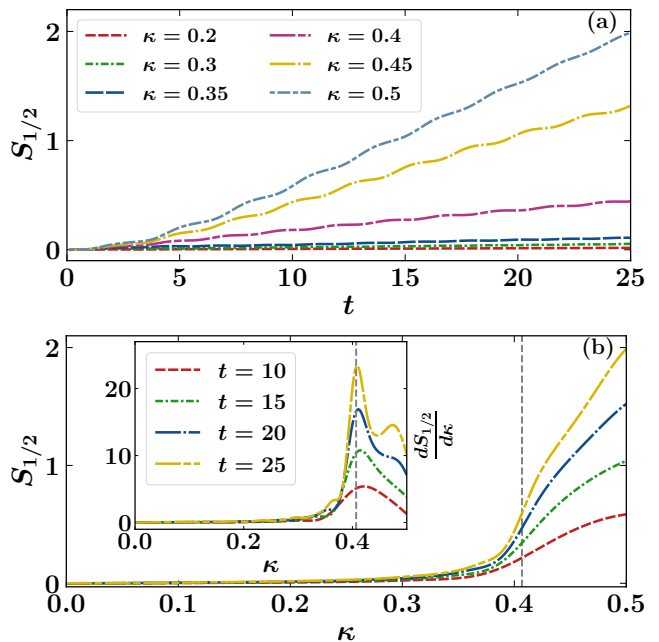


FIG. 4. Ferromagnetic to paramagnetic quantum phase transition in the ANNNI chain as revealed via real time dynamics of the half-chain entanglement entropy $S_{1/2}$. (a) Time evolution of $S_{1/2}$ for six values of κ . (b) $S_{1/2}$ at different times plotted as a function of κ . (Inset) Derivative with respect to κ of the results shown in the main panel. The initial state for the dynamics is the ground state of the ANNNI Hamiltonian with $\Gamma = 0.2$ and $\kappa_I = 0$. The vertical dashed lines mark the critical $\kappa_c \approx 0.41$.

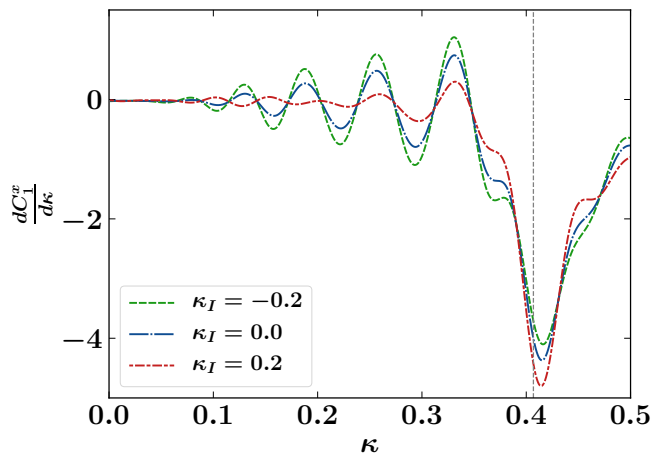


FIG. 5. Results for $dC_1^x/d\kappa$, as those in the inset in Fig. 3(a), obtained at a fixed time $t = 15$ after the quench for different values of κ_I ($-0.2, 0, 0.2$) in the initial ground state. The vertical dashed line marks the critical $\kappa_c \approx 0.41$.

A. Changing κ_I

In Fig. 5, we show the derivative of C_1^x with respect to κ at a fixed time after the quench, plotted as a function of κ , for different values of κ_I in the initial ground state. We recall that as κ_I departs from κ_c , for $\kappa_I < \kappa_c$, the ground state of the system is deeper in the ferromagnetic phase. The results in Fig. 5 show that starting deeper in the ferromagnetic phase results in a slightly shallower dip in $dC_1^x/d\kappa$, while its position remains unchanged. This might be expected as the departure of κ_I from κ_c increases the magnitude of the quench, and hence increases the final energy density, thereby blunting the signature of the quantum phase transition. This is consistent with the results in Sec. IV C, where we discuss the effect that the increase in the magnitude of the quench has in observables after thermalization.

IV. LONG-TIME THERMAL RESULTS

Because of the linear growth of the entanglement entropy seen in Fig. 4, the iTEBD technique only allows one to study dynamics at short and intermediate times. To explore the fate of observables after thermalization, we use a numerical linked cluster expansion (NLCE) [13]. We broaden the class of initial states to explore how initial nonzero temperatures modify the behavior of observables after thermalization.

Here we consider more general quenches within the ANNNI Hamiltonian involving initial states $\hat{\rho}_I$ that are thermal equilibrium states of the initial Hamiltonian $\hat{H}(\kappa_I)$. For an initial temperature T_I , $\hat{\rho}_I$ has the form

$$\hat{\rho}_I = \frac{e^{-\hat{H}(\kappa_I)/T_I}}{\text{Tr}[e^{-\hat{H}(\kappa_I)/T_I}]} \quad (4)$$

When $T_I = 0$, $\hat{\rho}_I$ is the ground state of $\hat{H}(\kappa_I)$. As in the previous section, we quench $\kappa_I \rightarrow \kappa$, while Γ is kept unchanged ($\Gamma = 0.2$). In Secs. IV A and IV B we fix $\kappa_I = 0$. In Sec. IV C, we explore what changes when κ_I is varied within the ferromagnetic phase ($\kappa_I < \kappa_c \approx 0.41$).

Since the energy after the quench is the only conserved quantity, at sufficiently long times in the thermodynamic limit, observables are expected to be described by a Gibbs ensemble [17]

$$\hat{\rho}_{\text{GE}}(\kappa) = \frac{e^{-\hat{H}(\kappa)/T(\kappa)}}{\text{Tr}[e^{-\hat{H}(\kappa)/T(\kappa)}]}, \quad (5)$$

with a temperature $T(\kappa) > 0$ (which is nonzero even when $T_I = 0$) determined by the energy $E(\kappa)$ set by the initial state $\hat{\rho}_I$, as dictated by:

$$\text{Tr}[\hat{\rho}_{\text{GE}}(\kappa)\hat{H}(\kappa)] = \text{Tr}[\hat{\rho}_I\hat{H}(\kappa)]. \quad (6)$$

We use the numerical linked cluster expansion (NLCE) technique introduced in Refs. [13] to study the thermal expectation values of observables in the thermodynamic limit. All the NLCE results reported in what follows are obtained using 15 orders of the maximally connected cluster expansion introduced in Refs. [22]. To gauge how well the series has converged, we estimate the convergence error for an observable by computing the relative difference between the last two orders (14 and 15) of the NLCE [22]. We only report results whose convergence error for the energy is less than 10^{-5} . $T(\kappa)$ is obtained by numerically matching the energies in the left and right side of Eq. (6). Both energies are evaluated using NLCE to 15 orders, and $T(\kappa)$ is computed by enforcing that their relative difference is less than 10^{-11} (see Ref. [22]). For observables other than the energy, we only report results whose convergence errors are less than 5×10^{-5} (except for the entropy, for which we set the cut off to be 7×10^{-5}). The convergence errors are small enough to be unimportant for the discussions that follow.

A. Observables

As mentioned before, in the thermodynamic limit at sufficiently long times after the quench, thermalization is expected to occur in the nonintegrable systems considered here [17]. Next we study the expected thermal equilibrium results that observables \hat{O} reach after equilibration following the quench.

In the space of all possible thermal equilibrium ensembles parameterized by the coordinates (T, κ) , the initial state $\hat{\rho}_I$ sets a trajectory $T(\kappa)$ determined by Eq. (6). One can then write

$$\frac{dO}{d\kappa} = \frac{dT}{d\kappa} \left(\frac{\partial O}{\partial T} \right)_\kappa + \left(\frac{\partial O}{\partial \kappa} \right)_T. \quad (7)$$

Since $O(T, \kappa)$ is an analytic function whenever $T > 0$, and since $dT/d\kappa$ is expected to be a smooth function of κ (we discuss this in Sec. IV B), then $dO/d\kappa$ must be

a smooth function of κ after equilibration following the quench. Still, for observables that are indicators of the quantum phase transition in nonintegrable systems (e.g., order parameters and related observables), $(\partial O/\partial T)_\kappa$ and $(\partial O/\partial \kappa)_T$ can be large if T is low when κ is close to κ_c (we show the latter to be the case for our quenches in Sec. IV B). This means that, even in thermal equilibrium, it is possible to have prominent (but smooth) features in $dO/d\kappa$ as observed at intermediate times in the previous section. In integrable systems, in which all possible states after equilibration are described by generalized Gibbs ensembles that are parameterized by extensive numbers of quantities [23, 24], nonanalytic behavior is possible and has in fact been observed in Refs. [6, 7].

In Fig. 6, we show the thermal equilibrium results obtained for the nearest C_1^x and next nearest C_2^x neighbor longitudinal spin correlations per site [see Eq. (3)] as functions of κ after the quench, as well as their expectation values in the ground state of $\hat{H}(\kappa)$ computed with iTEBD. The main panels show $dC_{1(2)}/d\kappa$, while the insets show $C_{1(2)}(\kappa)$, for various initial temperatures T_I and in the ground state (dotted lines, computed with iTEBD). In the ground state, C_1^x and C_2^x are nearly one in the ferromagnetic phase and exhibit a rapid decrease when crossing the quantum phase transition (prominent

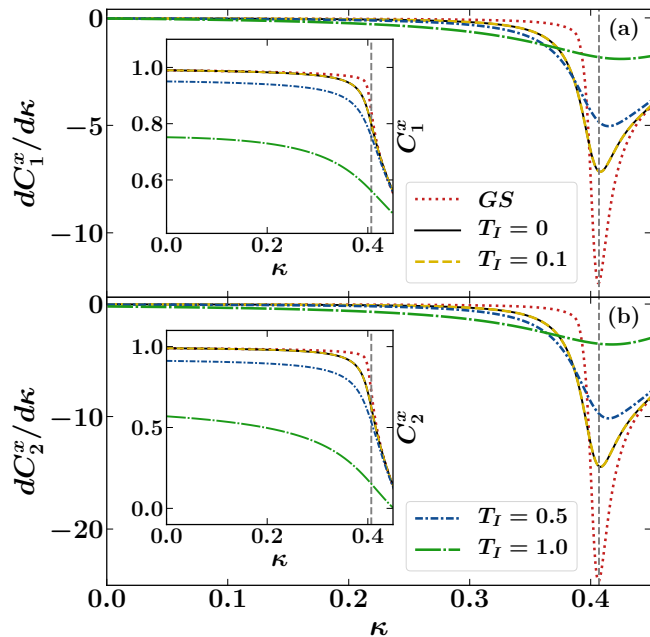


FIG. 6. The nearest (next nearest) neighbor longitudinal spin-spin correlation per site C_1^x (C_2^x), see Eq. (3), evaluated in thermal equilibrium using NLCE following quenches $\kappa_I = 0 \rightarrow \kappa$, with $T_I = 0, 0.1, 0.5$, and 1.0 . We also show C_1^x and C_2^x in the ground state of $\hat{H}(\kappa)$ (dotted lines) computed using iTEBD. The main panels in (a) and (b) show $dC_1/d\kappa$ and $dC_2/d\kappa$, respectively, while the corresponding insets show C_1^x and C_2^x . The vertical dashed lines mark the critical $\kappa_c \approx 0.41$.

minima can be seen in $dC_{1(2)}/d\kappa$ at κ_c , i.e., they serve as indicators of the quantum phase transition. (They also serve as indicators of the ferromagnetic to paramagnetic quantum phase transition in the integrable transverse field Ising model, see Appendix A.) This zero-temperature behavior is the precursor of the behavior of C_1^x and C_2^x observed in the insets for low initial T_I , which, in turn, produces the prominent minima in $dC_{1(2)}/d\kappa$ near κ_c observed in the main panels. Figure 6 shows that the position of the minima drift away from κ_c , and they become shallower, with increasing T_I . Note that the results for $T_I = 0$ and $T_I = 0.1$ are indistinguishable in the plots.

Qualitatively similar results were obtained for other local observables, such as the transverse magnetization per site $m^z = \sum_i \sigma_i^z/L$, shown in Fig. 7(a), and for the (von-Neumann) entropy per site s of the thermal state $\hat{\rho}_{GE}(\kappa)$, shown in Fig. 7(b). In the ground state, m^z increases rapidly when transitioning from the ferromagnetic to the paramagnetic phase, as shown in Fig. 7(a) (dotted lines, computed with iTEBD). Hence, m^z serves as an indicator of the quantum phase transition, and its behavior at zero temperature is the reason there are prominent maxima in $dm^z/d\kappa$ near κ_c for quenches at low T_I . (See Appendix A for ground state results of m^z across the ferromagnetic to paramagnetic quantum phase transition in the integrable

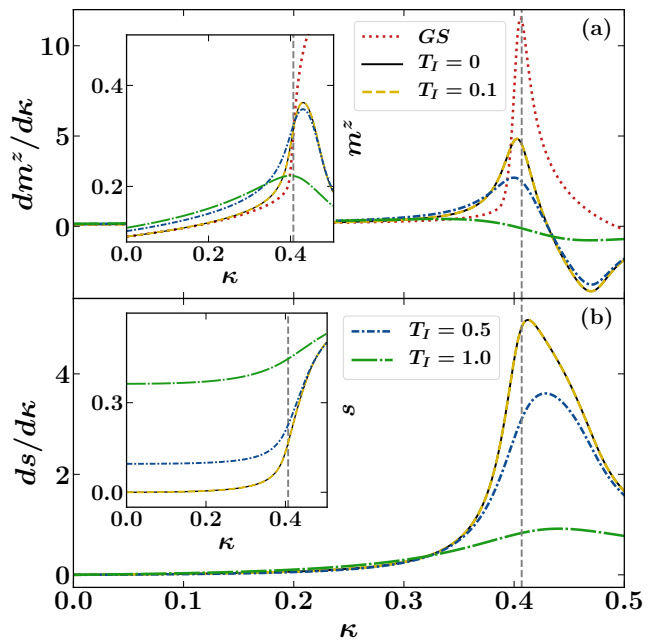


FIG. 7. The transverse spin magnetization (von-Neumann entropy) per site m^z (s), see text, evaluated using NLCE in thermal equilibrium following quenches $\kappa_I = 0 \rightarrow \kappa$ with $T_I = 0, 0.1, 0.5$, and 1.0 . The main panels in (a) and (b) show $dm^z/d\kappa$ and $ds/d\kappa$, respectively, while the corresponding insets show m^z and s . In (a), we also show results for m^z in the ground state of $\hat{H}(\kappa)$ (dotted lines) computed using iTEBD. The vertical dashed line marks the critical $\kappa_c \approx 0.41$.

transverse field Ising model.) The entropy, on the other hand, is strictly zero at zero temperature, i.e., it does not change at the phase transition [the entanglement entropy does change, as shown in Fig. 4(b)]. However, as we show in Sec. IV B, when T_I is low, the temperature after quench increases rapidly when κ crosses κ_c and this produces the rapid increase of s seen in Fig. 7(b).

B. Temperature

Let us now show that $dT/d\kappa$ is a smooth function of κ . The ANNNI Hamiltonian can be written as $\hat{H}(\kappa) = \hat{H}_0 + \kappa\hat{V}$, so that keeping the initial state $\hat{\rho}_I$ fixed and changing κ after the quench results in $E(\kappa)$ being a linear function of κ

$$E(\kappa) = \left(\text{Tr}[\hat{\rho}_I \hat{H}_0] \right) + \kappa \left(\text{Tr}[\hat{\rho}_I \hat{V}] \right), \quad (8)$$

with a slope $A \equiv dE(\kappa)/d\kappa = \text{Tr}[\hat{\rho}_I \hat{V}]$.

As in the previous section for $dO/d\kappa$, for the energy one can write

$$\frac{dE}{d\kappa} = \frac{dT}{d\kappa} \left(\frac{\partial E}{\partial T} \right)_{\kappa} + \left(\frac{\partial E}{\partial \kappa} \right)_{T}, \quad (9)$$

where $(\partial E/\partial T)_{\kappa} = C_{\kappa}(T)$ is the specific heat. Combining Eqs. (8) and (9), we have that

$$\frac{dT(\kappa)}{d\kappa} = \frac{A - \left(\frac{\partial E}{\partial \kappa} \right)_{T(\kappa)}}{C_{\kappa}[T(\kappa)]}. \quad (10)$$

All functions in the r.h.s. of Eq. (10) are smooth, and $C_{\kappa}[T(\kappa)] > 0$, because $T(\kappa) > 0$ after the quench. This shows that $T(\kappa)$ is also a smooth function. Next, we use numerical calculations to explore whether quenches $\kappa_I \rightarrow \kappa$ spanning across κ_c produce temperatures $T(\kappa)$ with signatures of the quantum phase transition, as shown to be the case in Sec. IV A for local observables.

Figure 8 shows $T(\kappa)$ for quenches with $\kappa_I = 0 \rightarrow \kappa$ for various initial temperatures T_I , including the ground state of $\hat{H}(\kappa_I)$. For very low initial temperatures $T_I \lesssim 0.1$, the temperatures $T(\kappa)$ after the quench are essentially indistinguishable from those for $T_I = 0$. This explains why all the results reported in Sec. IV A are indistinguishable for $T_I = 0$ and $T_I = 0.1$. For those very low T_I , the temperatures $T(\kappa)$ exhibit a low-temperature minimum in the vicinity of κ_c [notice that $T(\kappa)$ lies between 0.05 and 0.1]. At $T_I = 0.5$, a temperature at which $T(\kappa)$ after the quench departs from the $T_I = 0$ result, a minimum in $T(\kappa)$ still remains visible close to κ_c . The locus of minima in $T(\kappa)$, shown as a dotted line for a large number of T_I , makes apparent that the minima remain close to κ_c as long as T_I remains low ($T_I \lesssim 1.0$). At higher initial temperatures, the minima depart from κ_c indicating that the information about κ_c is washed out.

Overall it is remarkable that, due to the presence of the phase transition (and the corresponding closing of

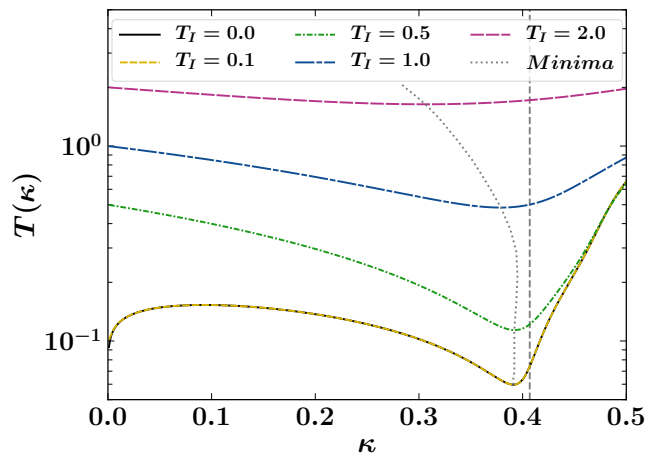


FIG. 8. NLCE results for the temperature of the Gibbs ensemble describing observables after equilibration, following quantum quenches $\kappa_I = 0 \rightarrow \kappa$ within the ANNNI Hamiltonian, for initial thermal states at different temperatures T_I . The locus of minima $[\kappa_m, T(\kappa_m)]$ for a large number of initial temperatures T_I is also shown. The vertical dashed lines mark the critical $\kappa_c \approx 0.41$.

the gap above the ground state), when quenching to the same (ordered) side of the critical point, the effective temperature decreases as the size of the quench increases and κ approaches the critical point. This trend sharply reverses as κ crosses the critical point.

Examining Eq. (10) in the context of our numerical results allows us to understand why a minimum develops near κ_c at very low ($T_I \lesssim 0.1$) and low ($T_I \lesssim 1.0$) initial temperatures. At the minimum, we have that

$$a = \left(\frac{\partial e}{\partial \kappa} \right)_{T}, \quad (11)$$

where we defined the intensive counterparts of the extensive quantities in Eq. (10) as $a = A/L$ and $e = E/L$.

The main panel in Fig. 9 shows $(\partial e/\partial \kappa)_T$ at different temperatures. For $T = 0$, we also show iTEBD results (the NLCE results do not converge close to $\kappa = \kappa_c$). Notice that, in the region in which the NLCE results converge to the precision mentioned in the introduction of this section, they are indistinguishable from the iTEBD ones. The iTEBD results for $(\partial e/\partial \kappa)_{T=0}$ exhibit a rapid decrease about κ_c (resulting in a singularity in $(\partial^2 e/\partial \kappa^2)_{T=0}$ at κ_c , Fig. 9, right inset), reflecting the nonanalytic behavior of the energy at the (second order) quantum phase transition. That rapid decrease leaves its signature in the low temperature behavior of $(\partial e/\partial \kappa)_{T>0}$, and this is what makes possible for Eq. (11) to be satisfied close to κ_c for low initial temperatures.

In Fig. 9, $a = \langle \sigma_i^x \sigma_{i+2}^x \rangle_{\hat{\rho}_I} / L$ is shown as a horizontal line for $T_I \lesssim 0.1$. For those very low initial temperatures, a is very close to 1 ($a \approx 0.99$) since $\kappa_I = 0$ is deep in the ferromagnetic phase, and Fig. 9 shows that the condition $(\partial e/\partial \kappa)_T = a$ is satisfied for κ very close to κ_c for temperatures between $T = 0.05$ and $T = 0.1$ (effective

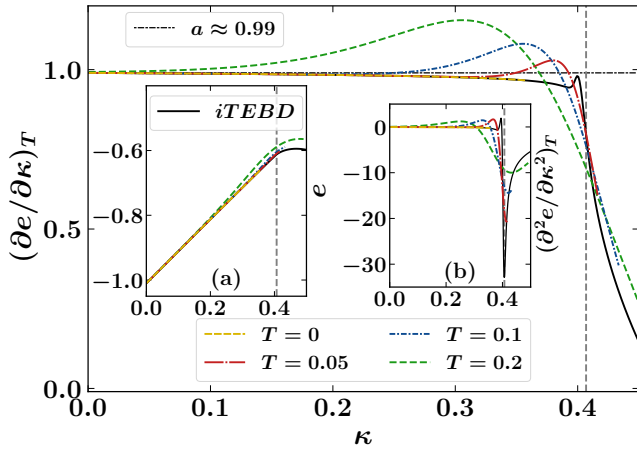


FIG. 9. Thermal equilibrium energy per site e and its derivatives at different T . (Main panel) $(\partial e/\partial\kappa)_T$, (left inset) e versus κ at constant temperature, and (right inset) $(\partial^2 e/\partial\kappa^2)_T$. Results are shown for different values of T (the main panel and the insets share the legend). The solid (black) curve ($T = 0$) shows the iTEBD results for the ground quantities, while the other curves show NLCE results. Also depicted in the main panel is $a = \langle \sigma_i^x \sigma_{i+2}^x \rangle_{\hat{\rho}_I} / L \approx 0.99$ for $T_I \lesssim 0.1$. The vertical dashed lines mark the critical $\kappa_c \approx 0.41$.

temperatures after the quench for κ close to κ_c when $T_I \lesssim 0.1$, see Fig. 8). This explains why the minimum in $T(\kappa)$ vs κ occurs very close to κ_c for $T_I \lesssim 0.1$. Increasing the initial temperature beyond $T_I = 0.1$ increases T but also reduces the value of a . This results in the minimum remaining close (and actually slightly approaching) κ_c in Fig. 8 when T_I departs from 0.1 but still remains low ($T_I \lesssim 1.0$). Since the slope of $(\partial e/\partial\kappa)_T$ at the crossing point near κ_c is negative, it follows from Eq. (10) that the extremum in $T(\kappa)$ near κ_c is a minimum.

C. Changing κ_I

Motivated by the results discussed in Sec. III A, we explore next what happens to the thermal equilibrium results after equilibration when one changes κ_I within the ferromagnetic regime, keeping $T_I = 0$ fixed. In Fig. 10(a), we show $T(\kappa)$ vs κ for $\kappa_I = -0.2, 0, \text{ and } 0.2$. As expected from the fact that the initial state remains a nearly perfect ferromagnet, the minima in $T(\kappa)$ close κ_c are robust to the choice of initial κ_I . However the minimum value of $T(\kappa)$ attained decreases as κ_I approaches κ_c . As a result, the signature of the presence of a quantum critical point in observables after thermalization becomes sharper as $\kappa_I \rightarrow \kappa_c$. This is apparent in Fig. 10(b) in which we plot $dC_1^x/d\kappa$.

Note that in Fig. 10(a) there is a singularity in $T(\kappa)$ at $\kappa = 0.2$ for $\kappa_I = 0.2$, as well as at $\kappa = 0$ for $\kappa_I = 0$. These are trivial consequences of performing no quench, which means that the system remains in the ground state. The fact that $|dT/d\kappa| \rightarrow \infty$ at those points follows from

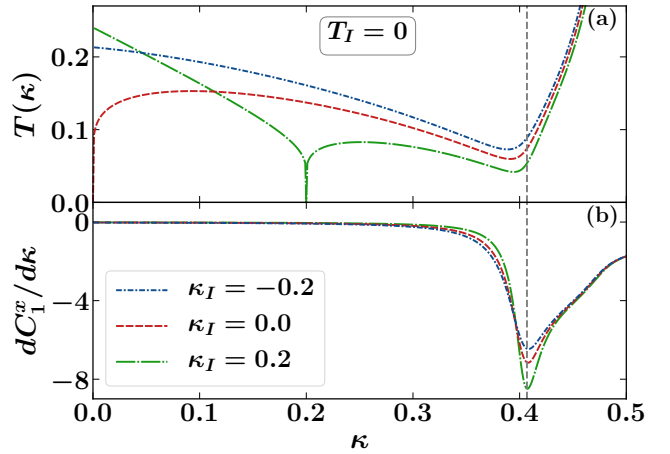


FIG. 10. (a) Equilibrium temperature $T(\kappa)$ and (b) $dC_1^x/d\kappa$ in thermal equilibrium, after quenches $\kappa_I \rightarrow \kappa$ from initial ground states of $\hat{H}(\kappa_I)$ for three different values of κ_I . The vertical dashed lines mark the critical $\kappa_c \approx 0.41$.

Eq. (10) due to specific heat $C_\kappa(T \rightarrow 0) \rightarrow 0$ in the denominator. These singularities have no consequence in the expectation values of observables.

V. PHASE DIAGRAM

Here we combine results obtained for C_1^x at intermediate times after the quench (from iTEBD calculations), and after equilibration (from NLCE calculations), to identify the phase boundary in the (κ, Γ) plane separating the ferromagnetic and paramagnetic phases in the ground state. We estimate κ_c by carrying out quenches $\kappa_I = 0 \rightarrow \kappa$ for different values of Γ (Γ is not changed during the quench). Qualitatively similar results were obtained for other local observables such as C_2^x and m^z and are not reported here.

In the main panel of Fig. 11, we show κ_c extracted from the extrema of $dC_1^x/d\kappa$ obtained using iTEBD results at $t = 25$ after quenches starting from the ground state, and NLCE thermal equilibrium results after quenches starting from the ground state ($T_I = 0$) and from an initial temperature $T_I = 0.3$. As Γ increases, the NLCE convergence errors are higher for quenches starting from the ground state. This occurs because the critical point gets closer to $\kappa_I = 0$ and the effective temperature after the quench becomes too small (see Fig. 10 and related discussion). This is the reason no NLCE points are reported for quenches with $\Gamma \geq 0.4$ and $T_I = 0$. On the other side of the phase diagram, when Γ is small, the quenches in κ result in fewer excitations ($\Gamma \rightarrow 0$ becomes the classical Ising chain) thereby bringing the thermal equilibrium ensemble about κ_c close to the ground state critical point. This also affects the NLCE convergence, resulting in no NLCE data points for $\Gamma \lesssim 0.2$. The results in Fig. 11 show that both the intermediate-time

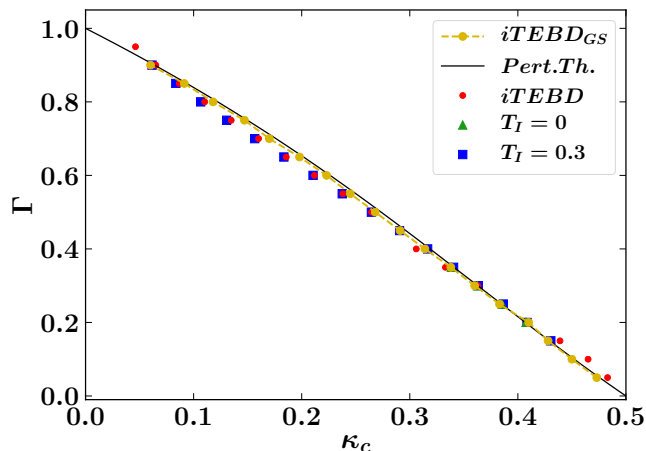


FIG. 11. Phase boundary for the ground state quantum phase transition in the (κ, Γ) plane separating the ferromagnetic and paramagnetic phases. Unbiased results for the boundary were obtained using ground-state iTEBD [iTEBD_{GS} in the legend, obtained locating the singularity in $(\partial^2 e / \partial \kappa^2)_{T=0}$] and are closely followed by the predictions of second order perturbation theory (continuous line). The phase boundary is well described by κ_c estimated from the extrema of $dC_I^x / d\kappa$ obtained in finite-time iTEBD calculations after the quench (for $\tau = 25$) and in the (expected) long-time thermal results obtained using NLCE. In all quenches $\kappa_I = 0 \rightarrow \kappa$, Γ is not changed during the quench, and we show results for $T_I = 0$ (iTEBD and NLCE), and for $T_I = 0.3$ (NLCE).

and (expected) long-time extrema follow very closely the phase boundary calculated using iTEBD for the ground state [locating the singularity in $(\partial^2 e / \partial \kappa^2)_{T=0}$], which is well described by the second order perturbation theory results.

VI. SUMMARY AND DISCUSSION

In summary, we have shown that local observables can be used to locate the ferromagnetic to paramagnetic quantum phase transition in the ANNNI chain (a nonintegrable model) both at intermediate times after a quench and at long times after thermalization. The initial states for our quenches were chosen to be ground states of the ANNNI chain deep in the ferromagnetic phase. We explored the effect that changing the magnitude of the quench and starting from initial finite temperature states has in many of our conclusions, and showed that our conclusions are robust against those changes.

The fact that intermediate-time dynamics, following quenches whose initial states are ground states far from a quantum phase transition, provide a way to locate the quantum phase transition is promising for experiments with ultracold quantum gases [3, 4] and ions [25, 26]. In those experiments, it is usually straightforward to prepare ground states far away from quantum phase transitions but it is much more challenging to prepare them

close to the transitions. The latter is needed to locate the quantum critical point via traditional measurements of the system in equilibrium. Also, not needing to wait long times to observe signatures of the quantum phase transition in the dynamics after the quench is important because, due to heating and other undesirable effects, keeping the dynamics coherent in the experiments becomes increasingly challenging as the evolution time increases.

We stress that the dynamics studied in this work is within reach in current experiments. In particular, the considered quantum quenches in the ANNNI model appear feasible using Rydberg dressing for ultracold atoms in optical lattices [27, 28]. Rydberg-dressed atoms exhibit a soft-core interaction potential, which is approximately constant below a threshold distance between two atoms and decays quickly beyond the threshold in a d^{-6} fashion as a function of distance d [27]. Thus, it is possible to tune the relative strength of nearest and next nearest neighbor interactions in such a way that further distant interactions can be approximately neglected due to the fast decay of the interaction potential at larger separations. Further, it is straightforward to also realize the necessary transverse field, to initialize the system in fully-polarized product states [27], and to measure the correlation functions defined in Eq. (3) [28].

An important question that we leave open to further exploration is how generally one can use our protocol to locate quantum phase transitions in other one-dimensional models. Given our results and insights gained within the ANNNI chain, we believe our protocol should be widely applicable to other one-dimensional models with traditional quantum phase transitions. A different question is whether it can be used to locate topological quantum phase transitions, as shown for non-interacting models in Ref. [7]. In what follows, we report results from a preliminary exploration of dynamics after quantum quenches about a topological transition in a quantum chaotic model.

We explored the quantum phase transition from the Néel to the symmetry protected topological “Haldane” phase in the spin-1 anisotropic (XXZ) Heisenberg chain model. The Hamiltonian for this model reads

$$\hat{H}_{\text{XXZ}} = \sum_i^L \left(\hat{S}_i^x \hat{S}_{i+1}^x + \hat{S}_i^y \hat{S}_{i+1}^y + \Delta \hat{S}_i^z \hat{S}_{i+1}^z \right), \quad (12)$$

where $\hat{S}_i^{x,y,z}$ denote the x , y and z components of the spin-1 operator at site i . Four different phases occur in this model when one changes the anisotropy parameter Δ (see, e.g., Refs. [29, 30] and references therein). Here we focus on the transition that occurs upon decreasing Δ from $\Delta > 1$, a limit in which \hat{H}_{XXZ} reduces to the spin-1 Ising antiferromagnet. With decreasing Δ , the ground state of \hat{H}_{XXZ} undergoes a quantum phase transition from the antiferromagnet to the Haldane phase at $\Delta_c \approx 1.183$. The Haldane phase is a topological phase, protected by any one of the following three global symme-

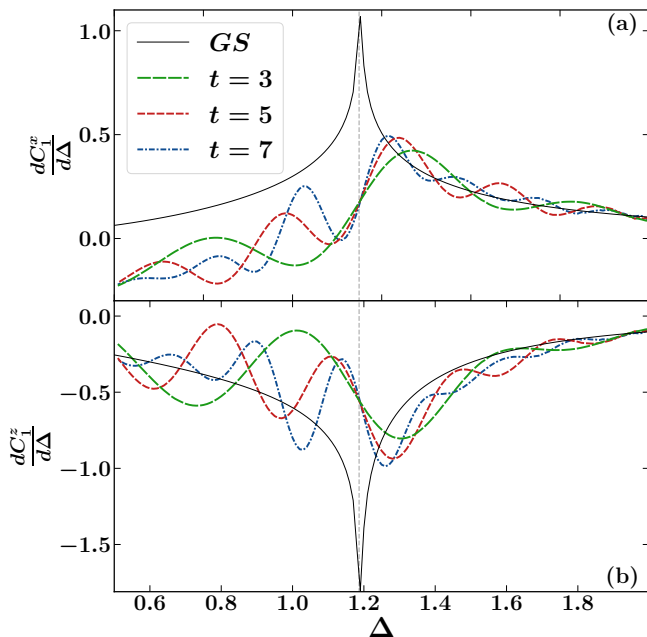


FIG. 12. Topological transition. Signature of the Néel to Haldane quantum phase transition in the anisotropic XXZ chain. Derivatives with respect to Δ of (a) C_1^x and (b) C_1^z at different fixed times after the quench, and of the results in the ground state (black solid line). The gray vertical line shows the critical $\Delta_c \approx 1.183$

tries: D_2 spin rotation, time-reversal, and bond centered inversion [31]. This transition is of second order, and belongs to the 2D Ising universality class [32, 33].

In our protocol, we start from the ground state at large $\Delta_I = 2$ and quench Δ across the neighborhood of Δ_c . Due to the high computational cost of the iTEBD calculations for the spin-1 anisotropic Heisenberg chain, we were only able to study dynamics at short times ($t \leq 7$) after the quench. Still, for these short times, Fig. 12(a) shows that a peak appears to develop with time in the derivative of the correlator C_1^x [see Eq. (3)], and Fig. 12(b) shows that a dip appears to develop in the derivative of the correlator

$$C_1^z = \frac{1}{L} \sum_{i=1}^L \langle \hat{S}_i^z \hat{S}_{i+1}^z \rangle, \quad (13)$$

with respect to Δ at fixed times. In Figs. 12(a) and 12(b), we also plot the derivatives of C_1^x and C_2^x , respectively, with respect to Δ in the ground state. The peak [Fig. 12(a)] and dip [Fig. 12(b)] seen there are expected to be the precursors of the features observed in the time evolution of those observables.

Thus the above results suggest that our protocol can also be used to locate topological quantum phase transitions (here transition from a Néel ordered phase to a topological phase) through the study of the quench dynamics of local operators. Further studies are needed to further explore this possibility.

ACKNOWLEDGMENTS

We thank F. Essler and R. Moessner for useful discussions. A.D. and A.H. acknowledge support from DST-MPI partner group program “Spin liquids: correlations, dynamics and disorder” between MPI-PKS (Dresden) and IACS (Kolkata), and the visitor’s program of MPI-PKS. K.M. and M.R. were supported by the National Science Foundation under Grant No. PHY-1707482. This research was supported in part by the International Centre for Theoretical Sciences (ICTS) during a visit for the program - Thermalization, Many body localization and Hydrodynamics (Code: ICTS/hydrodynamics2019/11). FP is funded by the European Research Council (ERC) under the European Unions Horizon 2020 research and innovation program (grant agreement No. 771537). FP acknowledges the support of the DFG Research Unit FOR 1807 through grants no.PO 1370/2-1, TRR80, and the Deutsche Forschungsgemeinschaft (DFG, German Research Foundation) under Germany’s Excellence Strategy EXC-2111- 390814868. This project has also received funding from the European Research Council (ERC) under the European Unions Horizon 2020 research and innovation programme (grant agreement No. 853443), and M. H. further acknowledges support by the Deutsche Forschungsgemeinschaft via the Gottfried Wilhelm Leibniz Prize program.

Appendix A: Integrable Transverse Field Ising Chain

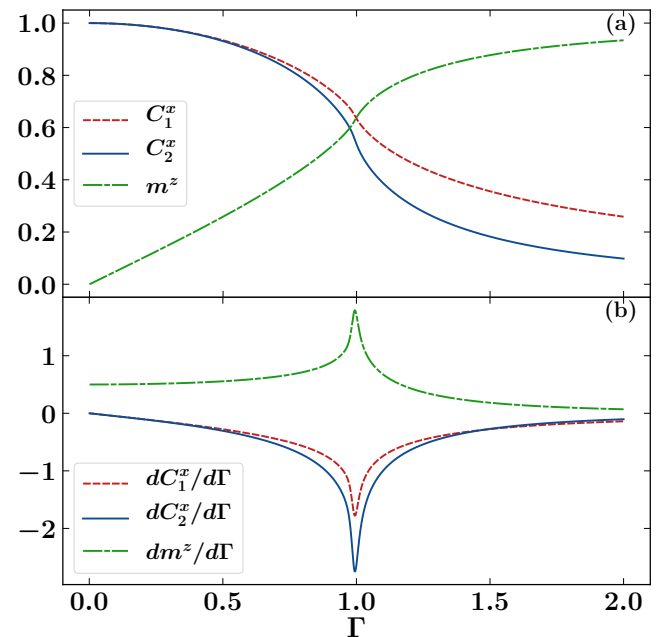


FIG. 13. Ground state results for (a) $C_{1(2)}^x$, and m_z , and (b) their derivatives, as functions of the strength of the transverse magnetic field.

The integrable transverse field Ising chain (TFIM) is probably the most studied exactly solvable model in the context of quantum phase transitions [1, 18]. Its Hamiltonian reads

$$\hat{H} \doteq - \sum_i^L \sigma_i^x \sigma_{i+1}^x - \Gamma \sum_i^L \sigma_i^z. \quad (\text{A1})$$

It is the noninteracting limit ($\kappa = 0$) of our ANNNI Hamiltonian [Eq. (1)].

In Fig. 13, we report ground state results for $C_{1(2)}$ and m_z [Fig. 13(a)], and their derivatives [Fig. 13(b)], across the ferromagnetic to paramagnetic phase transition, which occurs in this model at $\Gamma = 1$.

-
- [1] S. Sachdev, *Quantum Phase Transitions* (Cambridge University Press, 2011).
- [2] L. D. E. Carr, *Understanding Quantum Phase Transitions (1st Ed.)* (Taylor and Francis, 2010).
- [3] I. Bloch, J. Dalibard, and W. Zwerger, *Rev. Mod. Phys.* **80**, 8855964 (2008).
- [4] T. Esslinger, *Annu. Rev. Condens. Matter Phys.* **1**, 129152 (2010).
- [5] A. Keesling, A. Omran, H. Levine, H. Bernien, H. Pichler, S. Choi, R. Samajdar, S. Schwartz, P. Silvi, S. Sachdev, P. Zoller, M. Endres, M. Greiner, V. Vuletić, and M. D. Lukin, *Nature (London)* **568**, 207211 (2019).
- [6] S. Bhattacharyya, S. Dasgupta, and A. Das, *Scientific Reports* **5**, 16490 (2015).
- [7] S. Roy, R. Moessner, and A. Das, *Phys. Rev. B* **95**, 041105(R) (2017).
- [8] P. Titum, J. T. Iosue, J. R. Garrison, A. V. Gorshkov, and Z.-X. Gong, *Phys. Rev. Lett.* **123**, 115701 (2019).
- [9] M. Heyl, F. Pollmann, and B. Dora, *Phys. Rev. Lett.* **121**, 016801 (2018).
- [10] G. Vidal, *Phys. Rev. Lett.* **91**, 147902 (2003); *Phys. Rev. Lett.* **93**, 040502 (2004); *Phys. Rev. Lett.* **98**, 070201 (2007).
- [11] U. Schollwöck, *Annals of Physics* **326**, 96 (2011).
- [12] J. Hauschild and F. Pollmann, arXiv:1805.00055 (2018).
- [13] M. Rigol, T. Bryant, and R. R. P. Singh, *Phys. Rev. Lett.* **97**, 187202 (2006); *Phys. Rev. E* **75**, 061118 (2007).
- [14] J. M. Deutsch, *Phys. Rev. A* **43**, 204662049 (1991).
- [15] M. Srednicki, *Phys. Rev. E* **50**, 8888901 (1994).
- [16] M. Rigol, V. Dunjko, and M. Olshanii, *Nature* **452**, 854 (2008).
- [17] L. D'Alessio, Y. Kafri, A. Polkovnikov, and M. Rigol, *Adv. Phys.* **65**, 233362 (2016).
- [18] S. Suzuki, J.-i. Inoue, and B. K. Chakrabarti, *Quantum Ising Phases and Transitions in Transverse Ising Models* (Springer, Heidelberg, 2013).
- [19] M. A. Cazalilla, R. Citro, T. Giamarchi, E. Orignac, and M. Rigol, *Rev. Mod. Phys.* **83**, 14051466 (2011).
- [20] M. Beccaria, M. Campostrini, and A. Feo, *Phys. Rev. B* **73**, 052402 (2006).
- [21] H. Kim and D. A. Huse, *Phys. Rev. Lett.* **111**, 127205 (2013).
- [22] M. Rigol, *Phys. Rev. Lett.* **112**, 170601 (2014); *Phys. Rev. Lett.* **116**, 100601 (2016).
- [23] M. Rigol, V. Dunjko, V. Yurovsky, and M. Olshanii, *Phys. Rev. Lett.* **98**, 050405 (2007).
- [24] L. Vidmar and M. Rigol, *J. Stat. Mech.* **2016**, 064007 (2016).
- [25] D. Leibfried, R. Blatt, C. Monroe, and D. Wineland, *Rev. Mod. Phys.* **75**, 281324 (2003).
- [26] R. Islam, E. E. Edwards, K. Kim, S. Korenblit, C. Noh, H. Carmichael, G.-D. Lin, L.-M. Duan, C.-C. J. Wang, J. K. Freericks, and C. Monroe, *Nat. Comm.* **2**, 377 (2011).
- [27] J. Zeiher, R. van Bijnen, P. Schau, S. Hild, J.-Y. Choi, T. Pohl, I. Bloch, and C. Gross, *Nature Physics* **12**, 10951099 (2016).
- [28] J. Zeiher, J.-y. Choi, A. Rubio-Abadal, T. Pohl, R. van Bijnen, I. Bloch, and C. Gross, *Physical Review X* **7**, 041063 (2017).
- [29] W. Chen, K. Hida, and B. C. Sanctuary, *Phys. Rev. B* **67**, 104401 (2003).
- [30] Y. Heng Su, S. Young Cho, B. Li, H.-L. Wang, and H.-Q. Zhou, *Journal of the Physical Society of Japan* **81**, 074003 (2012).
- [31] F. Pollmann, E. Berg, A. M. Turner, and M. Oshikawa, *Phys. Rev. B* **85**, 075125 (2012).
- [32] T. Sakai and M. Takahashi, *Journal of the Physical Society of Japan* **59**, 26882693 (1990).
- [33] K. Nomura, *Phys. Rev. B* **40**, 91429146 (1989).